



# TPMS\_Scaffold\_Generator: A Scaffold-Structure Generator Based on Triply Periodic Minimal Surfaces

Di Lin<sup>a</sup>, Cong Zhang<sup>a,\*</sup>, Xiyong Chen<sup>b</sup>, Nannan Wang<sup>b</sup>, Lei Yang<sup>a,c,\*</sup>

<sup>a</sup> School of Transportation and Logistics Engineering, Wuhan University of Technology, Wuhan, 430070, China

<sup>b</sup> MOE Key Laboratory of New Processing Technology for Non-ferrous Metals and Materials, Guangxi Key Laboratory of Processing for Non-ferrous Metals and Featured Materials, Guangxi University, Nanning, 530004, China

<sup>c</sup> State Key Laboratory of Materials Processing and Die & Mould Technology, School of Materials Science and Engineering, Huazhong University of Science and Technology, Wuhan, 430074, China



## ARTICLE INFO

### Keywords:

TPMS scaffold generator  
Ultra-light scaffolds  
Triply periodic minimal surfaces (TPMS)  
Multisymmetrical scaffolds

## ABSTRACT

With the rapid development of additive manufacturing (AM), scaffold architectures based on triply periodic minimal surfaces (TPMS) have attracted increasing interest in various engineering fields. Nevertheless, they are limited because of the complexity of the design process when adopted in different research and engineering fields. In this work, we present a free and easy-to-use software package called TPMS\_Scaffold\_Generator, which is coded using MATLAB (Mathworks, Inc., USA). It offers three function tabs which are homogeneous tab, heterogeneous tab and multisymmetrical tab, respectively. Variables of the tabs include the volume fraction, topology type, unit cell size, the length of architecture in X, Y, Z direction, accuracy, and the style of gradient and so forth. TPMS\_Scaffold\_Generator can generate various TPMS scaffolds, especially ultralight and multisymmetrical scaffolds. The latest version of the TPMS\_Scaffold\_Generator is freely available at: [https://github.com/LeveeLin/TPMS\\_Scaffold\\_Generator.git](https://github.com/LeveeLin/TPMS_Scaffold_Generator.git).

## 1. Introduction

Cellular materials have been widely investigated for their superior properties, such as light weight, load bearing, damping, strain isolation, energy absorption, crack arresting, and self-healing [1]. The representative cellular materials, cellular solids, such as cork, wood, sponge, and trabecular bone, are composed of an interconnected array of struts or sheets. Their architecture can be obtained through either open- or closed-cell types connected in an orderly, periodic, or stochastic manner [2].

In addition, honeycombs [3] and foam [4] are engineering cellular solids that have been commonly used over the past two decades. The honeycomb cellular architecture, which can be designed as a two-dimensional template and extruded in a third direction, originates from honeycombs in nature. Unlike honeycombs, foam is a three-dimensional cellular material that contains complex cell geometries [5]. However, their widespread adoption is hindered by unavoidable process-related defects, the restricted control over foam's morphology, and the honeycomb's simplex two-dimensional architecture. With the development of additive manufacturing, triply periodic minimal surface (TPMS) scaffolds offer useful methods to solve these problems [6].

TPMS-based scaffolds are useful in many engineering applications and industries, such as construction [7,8], electrical [9], acoustic [10], transportation [11–13], chemical [14], optical [15] and energy [16]. The surfaces of such architectures are smooth, without edges or corners. This feature decreases the stress concentration observed in typical lattice network structures [17]. In addition, TPMS-based porous scaffolds have a wide range of fascinating topological features, such as bioinspired morphology, length scales, and structurally controlled characteristics. Therefore, these scaffolds exhibit excellent characteristics, including a high stiffness-to-weight ratio, heat-dissipation control, and enhanced mechanical-energy absorption [18]. Geometric features, such as the cell size, topology, and volume fraction [19] are the main factors controlling the mechanical and physical properties of these cellular materials [20].

Moreover, in additive manufacturing (AM), TPMS-based scaffolds can offer lightweight yet strong interior support to the boundary of a printed model. TPMS-based porous scaffolds can be further classified as skeleton-based and shell-based. As a result, a number of variables, including the scaffold type, unit-cell topology type, unit-cell size, and percent porosity, can be used to design a scaffold that meets different engineering requirements. Relevant software must be designed to bet-

\* Corresponding authors.

E-mail addresses: [zhangcong@whut.edu.cn](mailto:zhangcong@whut.edu.cn) (C. Zhang), [lei.yang@whut.edu.cn](mailto:lei.yang@whut.edu.cn) (L. Yang).

ter investigate the mechanical and physical properties of TPMS-based scaffolds.

On the one hand, as a consequence of the outstanding performance of TPMS-based scaffolds, a number of computer-aided-design (CAD) programs have been developed for scaffold-architecture generation. Many powerful commercial software packages exist, such as the Autodesk Netfabb software [21], Materialise 3-matic, the Materialise Magics Structures Module [22], and nTopology [23]. They feature lattice generation and provide considerable freedom in lattice design. However, they are so expensive that researchers have difficulty investigating the relationship between the geometric parameters and properties of TPMS-based scaffolds.

On the other hand, Autodesk provides a free software package called Meshmixer [24], which provides limited lattice-design abilities that help with AM build preparation, stereolithography (STL) file repair, orientation optimization, support generation, etc. [25]. Some helpful and free software packages are also available, including the MATLAB-based STL Lattice Generator [26], Minisurf [27], FLatt Pack [25] and MSlattice [28].

Among them, the Lattice Generator and Minisurf are open source, which greatly helps researchers to study the principles of generating TPMSs and their scaffolds. Unfortunately, they both have minimal functionality, which makes it difficult for researchers to further investigate the structure–property relationships.

Both FLatt Pack and MSlattice are powerful software packages with good scaffold visualization and optional variables, such as cell size, topology type, and scaffold volume fraction. Although MSlattice offers flexibility in allowing users to design their own TPMS lattice, based on level-set approximations, it is difficult for users to build a hybrid of two different scaffolds because of the difficulties in finding suitable level-set approximations and adjusting variables. Hence, a simple, easy-to-use, and affordable software package for designing and generating TPMS-based scaffolds is still lacking.

To better understand the material–topology–property relationship that can be used to control the functionality of a scaffold architecture or component, we propose TPMS\_Scaffold\_Generator. It offers many options for significant variables. Using this software, users can adjust the scaffold type, unit-cell topology type, unit-cell size, percent porosity, and accuracy. In addition, because AM provides access to scaffold architectures, TPMS\_Scaffold\_Generator offers homogeneous, heterogeneous and multisymmetrical tabs. Users can generate a uniform TPMS-based scaffold using the homogeneous tab. In the heterogeneous tab, users can generate graded scaffolds whose gradients can be in the volume fraction, cell size, or heterostructure. And, two- and four-fold symmetrical TPMS scaffolds can be created by users in the multisymmetrical tab.

In this study, we describe TPMS\_Scaffold\_Generator. TPMSs are introduced in [Section 2.1](#) because they are significant structures for designing functional porous scaffold architectures, owing to the advent of additive-manufacturing techniques [29]. Functionally graded TPMS structures are characterized by various structures and mechanical properties, thereby presenting better mechanical properties than homogeneous structures. Gradient strategies for the volume fraction, cell size, and cell-topology type are introduced in [Section 2.3](#).

## 2. Methodology

### 2.1. Triply periodic minimal surfaces

Generally, a minimal surface is defined as a surface in which the mean curvatures vanish at every point. A minimal surface that is infinite and periodic in three independent directions is called a triply periodic minimal surface (TPMS) [18]. A surface is a set of points with a constant function value. A zero-valued surface, known as a zero or level set, represents the interface regions of the space lying on, inside, or outside the space [30].

TPMS\_Scaffold\_Generator has eight built-in TPMSs, including the primitive (P) and diamond (D) surfaces discovered by Schwarz [31], and the gyroid (G), I-graph and wrapped package-graph (IWP), face-centered cubic rhombic dodecahedron (FRD), Neovius (N), Fischer-Koch (F), and lidinoid (L) surfaces [32]. They can be approximated by the level-set surfaces of trigonometric functions [33–35] listed in [Table 1](#).

In these equations,  $X$ ,  $Y$ , and  $Z$  refer to  $2\pi x/a$ ,  $2\pi y/a$ , and  $2\pi z/a$ , respectively. Moreover, the constant  $t$  controls the volume surrounded by the cell surface, as well as the position of the boundary between two subdomains [36]. Parameter  $a$  is the unit-cell size [32,37]. As shown in [Fig. 1](#), eight TPMSs were generated using MATLAB (Mathworks, Inc., USA).

### 2.2. Design of uniform scaffold structures

TPMS-based scaffolds can be classified into two main types, as shown in [Fig. 2](#): skeleton- and shell-based scaffolds [38]. Hence, two methods have been reported for generating TPMS-based structures. These methods rely on determining the isosurface (a surface that follows a constant value within a three-dimensional function) using the marching-cubes algorithm [39].

The first strategy yields shell-based scaffold architectures by thickening the minimal surface, where the thickness is continuous and fixed throughout the surface, as shown in [Fig. 2\(a\)](#). The other strategy produces skeleton-based scaffold structures by solidifying the volumes enclosed by the TPMSs [40,41]. The methods for creating these two types of scaffolds will be introduced in [Sections 2.2.1](#) and [2.2.2](#).

#### 2.2.1. Design of shell-based scaffold structures

As introduced above, we can provide the TPMS with an exact thickness by defining the expression  $-t < U < t$  to mathematically create shell-based scaffold architectures. In this study, as shown in [Fig. 2\(b\)](#), eight types of shell-based scaffolds were built using TPMS\_Scaffold\_Generator. The scaffold structures' volume fraction  $\varphi$ , defined as the ratio of the architectures' volume to the space cubic volume, is related to the value of  $t$  (The Materialise Magics software package can show the volume after repairing a model). This relationship can be determined by function fitting both parameters.

Because the volume fraction is an input parameter of the software,  $\varphi$  is set as an independent variable, while  $t$  is set as a dependent variable. According to this method, the scatter plots, fitting equations, and ranges of different styles of volume fractions are presented in Supporting Information 1. Because shell-based architectures have an exact thickness, pinch-off problems do not exist. When the  $t$  value is outside the range listed in Supporting Information Part 1, the generated scaffold will be distorted or far from the expected shape. That is, the expected model can only be obtained for a given volume-fraction range.

#### 2.2.2. Design of skeleton-based scaffold structures

A TPMS can partition a symmetrical space into two subdomains. One of them is solidified by mathematically determining  $U > t$  or  $U < -t$  to obtain skeleton-based scaffold structures; the other is a void district. As shown in [Fig. 2\(c\)](#), the generator was utilized to produce eight types of skeleton-based scaffold architectures [18]. Because the volume fraction of the scaffold structures is controlled by the offset value  $t$ , both variables can be function-fitted to determine their relationship. The relationship between the value of  $t$  and the volume fraction of the scaffolds was specifically investigated, and the details are presented in Supporting Information Part 2.

### 2.3. Generation of functionally-graded porous scaffolds

The proposed generator can grade the volume fraction, unit-cell size, and multi-morphology (of hybrid scaffolds) of skeleton- and shell-based scaffolds. Porous scaffolds, functionally graded in terms of cell size, are

**Table 1**  
Eight types of level-set surfaces of trigonometric functions.

Styles	Trigonometric equations
$U_P$	$\cos X + \cos Y + \cos Z - t = 0$
$U_D$	$\sin X \sin Y \sin Z + \sin X \cos Y \cos Z + \cos X \sin Y \cos Z + \cos X \cos Y \sin Z - t = 0$
$U_G$	$\sin X \cos Y + \sin Y \cos Z + \sin Z \cos X - t = 0$
$U_{IWP}$	$2(\cos X \cos Y + \cos Y \cos Z + \cos Z \cos X) - (\cos X + \cos Y + \cos Z) - t = 0$
$U_{FRD}$	$8(\cos X \cos Y \cos Z + \cos 2X \cos 2Y \cos 2Z) - (\cos 2X \cos 2Y + \cos 2Y \cos 2Z + \cos 2Z \cos 2X) - t = 0$
$U_N$	$3(\cos X + \cos Y + \cos Z) + 4(\cos X \cos Y \cos Z) - t = 0$
$U_F$	$\cos 2X \sin Y \cos Z + \cos 2Y \sin Z \cos X + \cos 2Z \sin X \cos Y - t = 0$
$U_L$	$0.5(\sin 2X \cos Y \sin Z + \sin 2Y \cos Z \sin X + \sin 2Z \cos X \sin Y) - 0.5(\cos 2X \cos 2Y + \cos 2Y \cos 2Z + \cos 2Z \cos 2X) + 0.15 - t = 0$

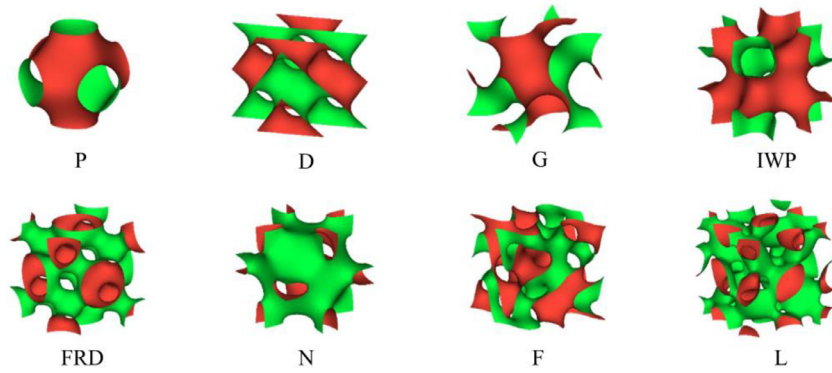


**Fig. 1.** Eight TPMSs, in which each unit cell is 1 mm × 1 mm × 1 mm and  $t = 0$ .

gaining increasing attention in the field of tissue engineering because the cell size varies in diverse places within biological skeletons. Compared with homogeneous architectures, scaffolds with graded cell sizes have better cell adhesion and growth on the bones.

### 2.3.1. Volume-fraction grading

As mentioned above, the volume fraction of TPMS-based scaffold architectures can be controlled by adjusting parameter  $t$  in the TPMS functions. The constant value  $t$  in the TPMS functions is replaced with  $t(x, y, z)$  to enable variations in the volume fraction throughout the scaffold architecture. According to these methods, two types of volume-fraction grading, linear and cosine, are introduced in Supporting Information Part 3.

### 2.3.2. Unit-cell size gradient

The designed software offers a linear gradient of cell-sized graded scaffolds.  $U_P$  is used as an example to show how the related gradient in cell-size graded scaffolds is generated. The corresponding equation is replaced with  $U_P$ :

$$\cos(\alpha X) + \cos(\beta Y) + \cos(\gamma Z) - t = 0 \quad (1)$$

The related parameters of Eq. (1) are identical to those of the level-set surfaces of trigonometric functions introduced in Section 2.1, whereas  $\alpha$ ,  $\beta$ , and  $\gamma$  are important variables that control the unit-cell size.

A comparison of the equations for  $U_P$  in Table 1 and Eq. (1) reveals that  $\alpha = \beta = \gamma = 1/a$  for uniform scaffolds. To obtain a linear gradient in cell-size graded scaffolds,  $a$  can be converted into a linear function, which also means the gradient can be created by defining  $\alpha$ ,  $\beta$ , and  $\gamma$  as a

function about  $x$ ,  $y$ , and  $z$ . After applying this method, we obtained a linear gradient in the cell-sized graded scaffolds; the details are presented in Supporting Information Part 4.

### 2.3.3. Multi-morphologically porous-scaffold design

Natural tissues with different forms cannot be represented by a homogeneous architecture; instead, most of them are multi-morphologically porous scaffolds [42]. Two CAD strategies combine different TPMS-based structures with the given transition boundaries. One is the sigmoid-function (SF) method [43,44] which can be effectively employed in ordinary transition-frontier cases. The other is the beta growth function (BGF) method, which can easily and accurately hybridize two distinct TPMS porous morphologies [45,46]. The proposed software employs the SF method. The main content of this method is presented in Supporting Information Part 5.

## 3. Fabrication and Results

After applying the mathematical expressions introduced in Section 2 to generate TPMS-based architectures using MATLAB (Mathworks, Inc., USA) software, the TPMS\_Scaffold\_Generator was written; it can be obtained from [https://github.com/LeveeLin/TPMS\\_Scaffold\\_Generator.git](https://github.com/LeveeLin/TPMS_Scaffold_Generator.git). The performance of this software is demonstrated in Supporting Information Part 6, and a 3D printed version of the model exported by TPMS\_Scaffold\_Generator is shown in Supporting Information Part 7.

To further demonstrate the practicability of this software, grade Fischer-Koch scaffolds were created and their mechanical properties were investigated.

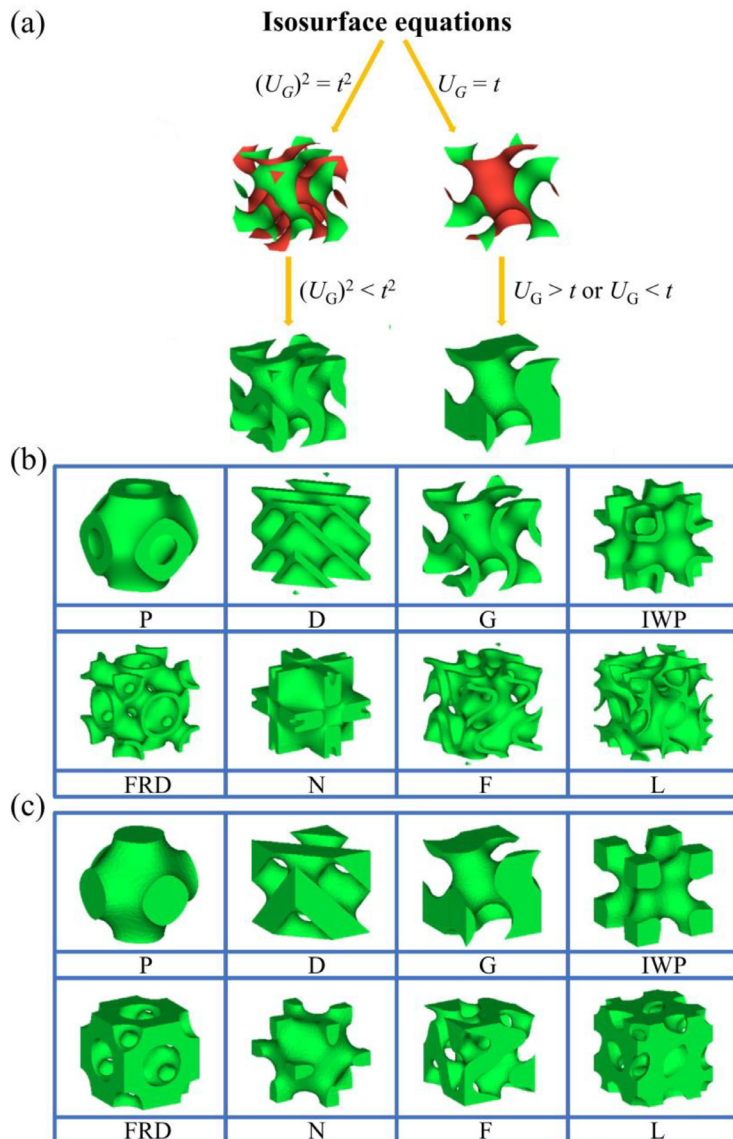


**Fig. 2.** (a) Illustration of the generation of shell-based and skeleton-based scaffolds; (b) Eight unit-cell types of shell-based scaffolds, in which each unit cell is  $1 \text{ mm} \times 1 \text{ mm} \times 1 \text{ mm}$  and the volume fraction is 30 %; (c) Eight unit-cell types of one skeleton-based scaffold in which each unit cell is  $1 \text{ mm} \times 1 \text{ mm} \times 1 \text{ mm}$  and  $t = 0$ .

### 3.1. Materials and fabrication process

The  $\text{Ti}_6\text{Al}_4\text{V}$  powder used in this study was produced using electrode-induction melting-gas atomization technology (Avimetal Powder Metallurgy Technology Co., Ltd., Beijing, China). A Quanta 650 field-emission gun (FEG) scanning electron microscope (SEM) (FEI, USA) was used to observe the morphology of the  $\text{Ti}_6\text{Al}_4\text{V}$  powder. As shown in Fig. 3(a), the  $\text{Ti}_6\text{Al}_4\text{V}$  particles were spherical or near-spherical with smooth surfaces. The particle-size distribution of the  $\text{Ti}_6\text{Al}_4\text{V}$  powder was measured using a Mastersizer-3000 laser particle-size analyzer (Malvern, England). The size of the  $\text{Ti}_6\text{Al}_4\text{V}$  particles ranged from  $23.8 \mu\text{m}$  to  $58.8 \mu\text{m}$  with an average size of  $37.7 \mu\text{m}$ , as illustrated in Fig. 3(b).

As shown in Figs. 3(c), (d), and (e), TPMS\_Scaffold\_Generator was used to create a uniform Fischer-Koch scaffold (U-FK), gradient Fischer-Koch scaffold along the Z axis (G1-FK), and gradient Fischer-Koch scaffold along the X axis (G2-FK). The  $\text{Ti}_6\text{Al}_4\text{V}$  Fischer-Koch TPMS scaffolds were fabricated using a commercial DiMetal-100H laser powder-bed fusion (L-PBF) machine (Guangzhou Laseradd Additive Technology Co., Ltd., Guangzhou, China) equipped with a 500 W ytterbium fiber laser. Its maximum scanning rate and minimum spot were  $7.8 \text{ m/s}$  and  $20 \mu\text{m}$ , respectively.

**Table 2**  
L-PBF parameters.

Parameter	Value
Laser power (W)	170
Scanning velocity (mm/s)	1100
Layer thickness ( $\mu\text{m}$ )	30
Hatch spacing ( $\mu\text{m}$ )	70
Hatch angle (°)	90
Volumetric energy density ( $\text{J/mm}^3$ )	73.59

The scaffolds were printed in a high-purity argon atmosphere, and the oxygen content in the building chamber was maintained below 300 ppm. Based on our ongoing experiments, we selected the L-PBF parameters listed in Table 2. The finished  $\text{Ti}_6\text{Al}_4\text{V}$  specimens were removed from the substrate using a Mo filament cutter and cleaned using an ultrasonic cleaner with absolute ethyl alcohol.

Fig. 3(f) presents general views of the samples fabricated using L-PBF. No broken struts or cells were observed in the as-prepared samples. This indicates that the  $\text{Ti}_6\text{Al}_4\text{V}$  Fischer-Koch TPMS scaffolds were well fabricated using the L-PBF parameters provided in Table 2.

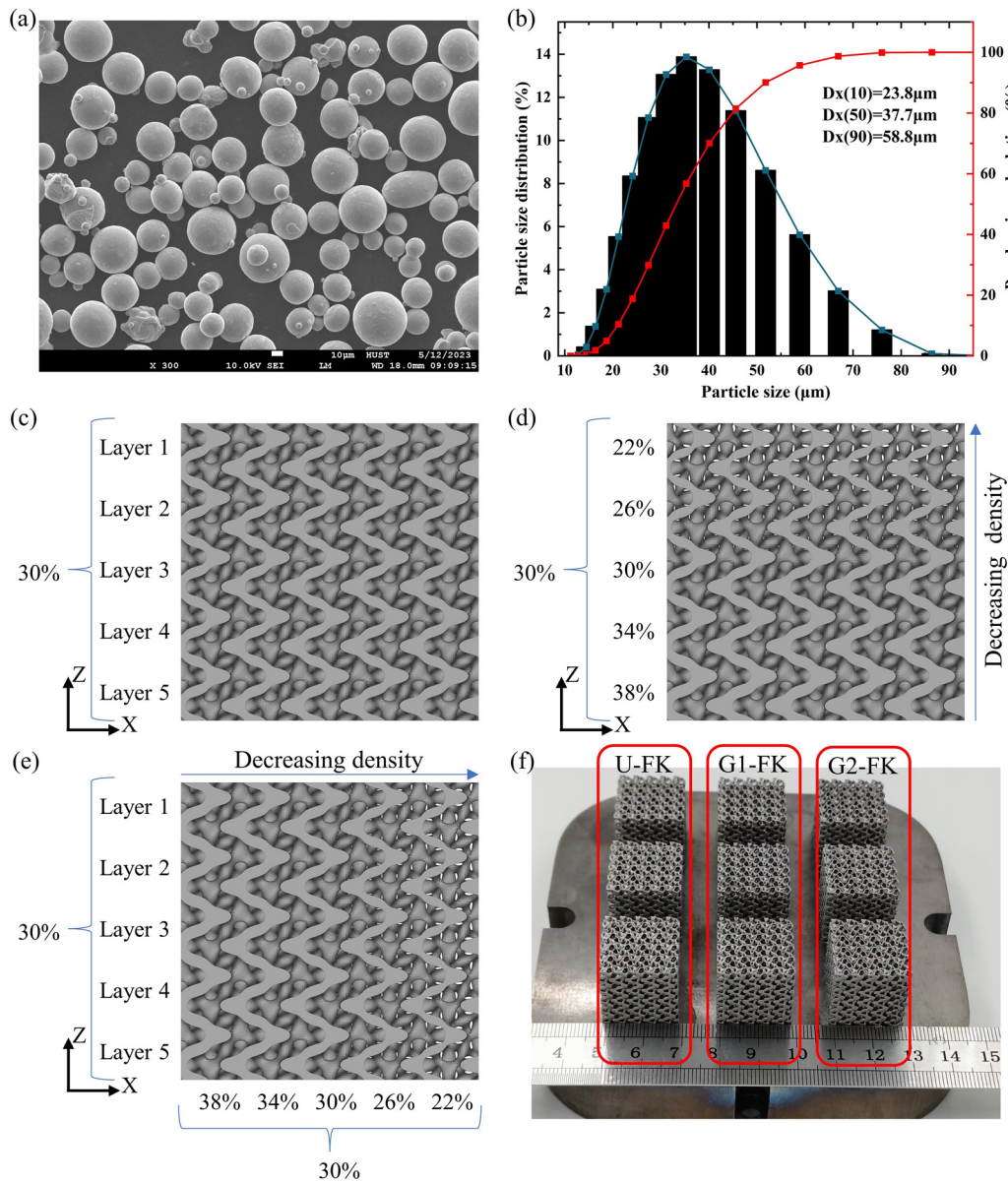


**Fig. 3.** (a) SEM image; (b) Particle-size distribution of Ti<sub>6</sub>Al<sub>4</sub>V powder; (c) 20 mm × 20 mm × 20 mm uniform Fischer–Koch scaffold with 4-mm unit-cell size; (d) 20 mm × 20 mm × 20 mm Z-oriented gradient Fischer–Koch scaffold with 4-mm unit-cell size; (e) 20 mm × 20 mm × 20 mm X-oriented gradient Fischer–Koch scaffold with 4-mm unit-cell size; (f) Photo of the L-PBF-fabricated Ti<sub>6</sub>Al<sub>4</sub>V Fischer–Koch TPMS scaffolds.

### 3.2. Measurements and characterization

The relative density (RD) of the solid struts of the Ti<sub>6</sub>Al<sub>4</sub>V Fischer–Koch TPMS scaffolds manufactured by L-PBF is defined as the ratio of the actual density to the theoretical density (4.45 g/cm<sup>3</sup>). The actual densities of the scaffolds fabricated by L-PBF were determined using the Archimedes method via a ME204 electronic balance with a 0.1 mg scale increment (Mettler Toledo, Switzerland).

The percentage deviation of the volume fraction between the Ti<sub>6</sub>Al<sub>4</sub>V Fischer–Koch TPMS scaffold fabricated by L-PBF and the designed CAD model was defined as the ratio of the difference between the actual and designed volume fractions to the designed volume fraction. The actual relative densities of the samples were obtained by dividing the actual volume of the solid struts of the as-built specimens by the total volume of the cubic samples. The actual volume of the solid struts was measured using the Archimedes method. The total volume of the cubic sample was calculated according to its overall dimensions, which were determined using a digital Vernier caliper with a 0.01 mm

increment (Greener, China). **Table 3** shows the measured dimensions, weights, and densities of the fabricated Fischer–Koch samples.

The mechanical behaviors of the Ti<sub>6</sub>Al<sub>4</sub>V Fischer–Koch TPMS scaffolds were investigated through uniaxial compression tests at room temperature (RT) along the building direction (Z-axis) at a 0.02 mm/s strain using an AG-IC 100 KN electronic universal-testing machine (Shimadzu, Japan). The applied loads were obtained to calculate the compressive stress by dividing the value of the load by the effective area of the scaffold structure. The strain was calculated by dividing the displacement of the upper compression die by the original height of the Ti<sub>6</sub>Al<sub>4</sub>V Fischer–Koch TPMS scaffold.

### 3.3. Deformation and collapse stages of the Fischer–Koch scaffolds

**Fig. 4** shows the deformation stages recorded by a high-speed camera for U-FK, G1-FK, and G2-FK at strain levels of 0%, 20%, 25%, 35%, and 45%. **Fig. 5** illustrates the experimental stress–strain curves of the Fischer–Koch scaffolds under a uniaxial compression test.

**Table 3**

Dimensions, weights, and densities of the fabricated Fischer–Koch samples.

Designed Scaffold	Actual dimensions of cellular cubic $X \times Y \times Z$ (mm)	Weight (g)	RD of Solid struts (%)	Actual RD $\rho$ (%)	Mean RD $\bar{\rho}$ (%)	Deviation $\eta RD$ (%)
U-FK (1)	20.23 × 20.20 × 20.18	12.32	98.1	33.87		
U-FK (2)	20.16 × 20.16 × 20.21	12.32	98.0	33.99	33.93	13.10
G1-FK (1)	20.15 × 20.16 × 20.19	12.38	98.1	34.18		
G1-FK (2)	20.17 × 20.16 × 20.17	12.29	98.2	33.86	34.02	13.41
G2-FK (1)	20.18 × 20.16 × 20.17	12.26	98.0	33.88		
G2-FK (2)	20.16 × 20.16 × 20.14	12.31	98.0	34.12	34.00	13.33

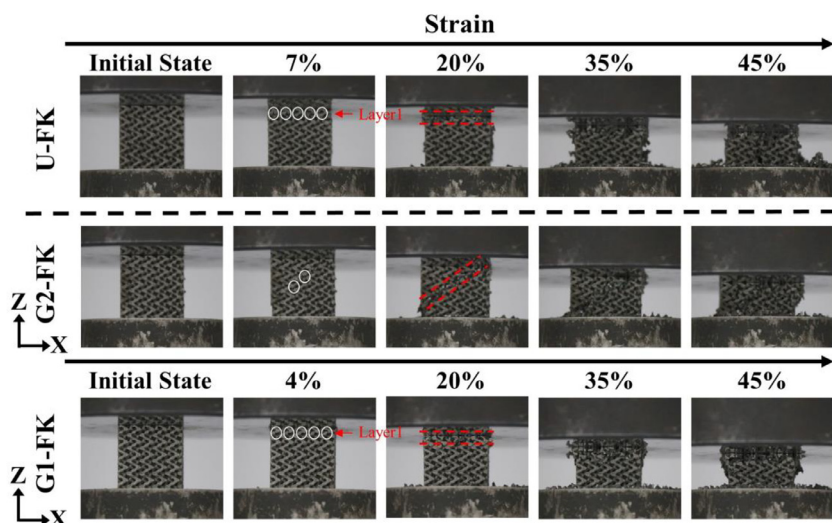


Fig. 4. Footage captured during uniaxial compression at different strain stages for three types of Fischer–Koch scaffolds.

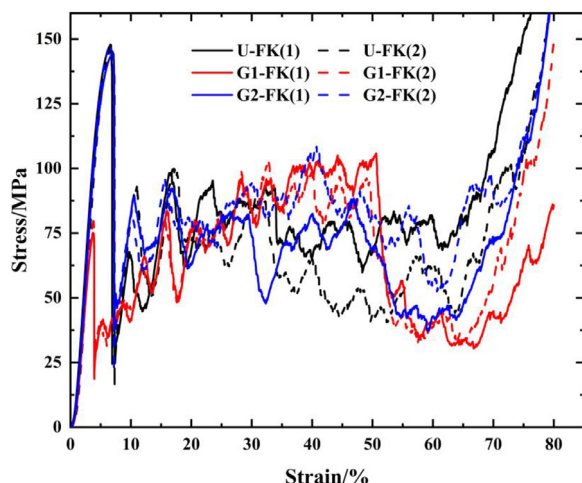


Fig. 5. Compressive stress–strain curves of Fischer–Koch scaffolds.

As shown in Fig. 4, for U-FK and G2-FK, the initial cracks (indicated by white circles) appeared in the first layer. It is noticeable that the crack in G1-FK initiated at a strain of only 4%, owing to the lower density in the first layer than that of U-FK. In addition, most cracks appeared in relatively thin struts.

With increasing compressive strain, both holistic structures exhibited layer-by-layer collapses. For G2-FK, the initial crack appeared at a strain of 7%, which was the same as its counterpart U-FK. This is because the densities of these two structures in each layer along the Z axis are identical. However, the fracture phenomena differ. U-FK shows a layer-by-layer collapse, whereas G2-FK has a nearly 45° fracture band. This is because the volume fraction of G2-FK along the X-axis changes in the X-Y plane.

As shown in Fig. 5, although the overall mechanical properties of the three types of samples are different, they exhibit similar four-stage mechanical responses. In the first stage, known as the elastic-deformation stage, the stress increases linearly with increasing strain, and the slope represents the compressive modulus.

The second stage is a linear–plastic deformation stage in which the stress–strain curve leaves the linear response. The nominal yield strength is determined by the stress at which the stress–strain curve for axial loading deviates by 0.2% from the linear–elastic region. In this linear–plastic deformation stage, the stress increases nonlinearly with an increase in the compression strain until it reaches the maximum stress, denoted as the ultimate strength. Subsequently, a noticeable decline in stress is observed in the stress–strain curve after a short yield plateau.

The stress–strain curve then enters the third stage, which is a long plateau region with fluctuating stress. Finally, a large number of struts in these structures are destroyed and squeezed together, and the stress–strain curve becomes denser, in which the stress increases as the strain rises.

In addition, it is clear from Fig. 5 that the deformation responses of U-FK and G2-FK are very similar, which is identical to the strain at which their initial cracks appear. This is because the density of each layer in both structures is uniform (30%). Nevertheless, the deformation response of G1-FK differs from those of the other two. Its ultimate strength is obviously lower than those of U-FK and G2-FK, mainly because the density of its first layer is relatively low, at 22%.

## 4. Discussion

### 4.1. Relationship between the accuracy and volume fraction

The obtained TPMS scaffold is highly dependent on the accuracy-controlling parameter, which is the number of mesh points in a unit.

The accuracy-controlling parameter is denoted by A in Figs. 6 and 7 is related to the volume fraction of the scaffold when the pinch-off prob-

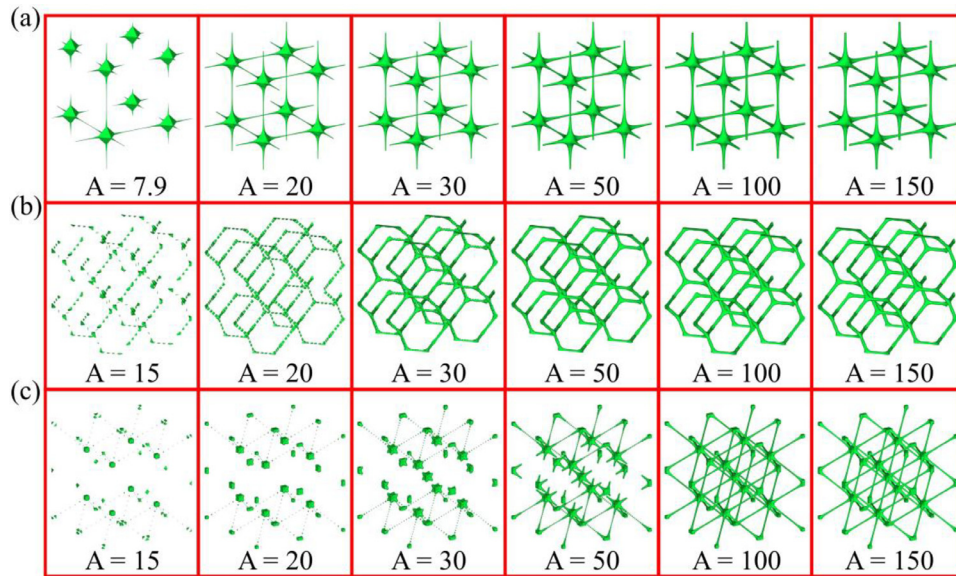


**Fig. 6.** Skeleton-based scaffolds whose volume fraction is set to 1%: (a) Primitive scaffolds; (b) Gyroid scaffolds; (c) IWP scaffolds.

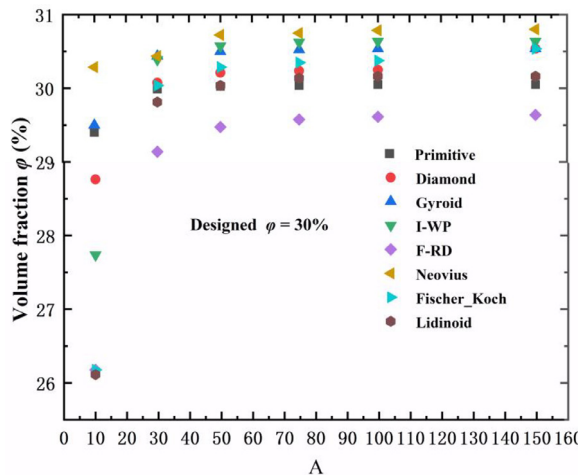


**Fig. 7.** Actual volume fraction of skeleton-based scaffolds with input parameter (volume fraction = 30%).

lem is investigated. When this software was used to create a skeleton-based IWP scaffold with a 1% volume fraction, the scaffold was discontinuous. However, this can be resolved by adjusting the accuracy to 100 or more. Therefore, we chose three groups of scaffolds with a wide range of accuracy values, as shown in Fig. 6.

Clearly, when the accuracy is too low, a discontinuity or pinch-off problem appears. For example, primitive scaffolds with  $A = 7.9$ , gyroid scaffolds with  $A = 15$  and 20, and IWP scaffolds with  $A = 15, 20, 30$ , and 50 are discontinuous. In addition, the volume fraction of these scaffolds is lower than anticipated (here, 1%). The volume fraction of scaffolds with high accuracy will increase subtly, with few effects on our anticipated targets. In conclusion, users can input a higher accuracy value to solve the discontinuity and obtain scaffolds with a low volume fraction.

It is also necessary to investigate the relationship between the accuracy and scaffolds with higher volume fractions; the related data are shown in Fig. 7. We can see from the chart that a higher accuracy has little effect on the volume fraction of the scaffolds; therefore, this phenomenon can be ignored.

When the accuracy is too low, two problems occur. First, the connections of the triangular patches are not sufficiently smooth because of the lower accuracy. Hence, the volume fraction of the scaffolds, includ-

ing the primitive, diamond, gyroid and I-WP, will be slightly lower than expected.

Secondly, a pinch-off problem occurs. For example, the volume fractions of F-RD, Fischer-Koch, and lidinoid (26.175%, 26.175%, and 26.1125%, respectively) were significantly lower than 30%. In other words, the scaffold becomes discontinuous when the accuracy is low, and the volume fraction of the scaffold appears to be lower than expected.

#### 4.2. Complicated TPMS scaffolds

##### 4.2.1. Multi-dimensional TPMS scaffolds

In addition to the functional method mentioned in Section 2.3.1, interpolation can be used to generate scaffolds with a linear gradient. In Fig. 8, linear-gradient IWP structures are used to demonstrate the results of the interpolation method. This method can flexibly generate multiple linear gradients within a structure, although many interpolation points must be provided so that ideal models can be obtained; this is inconvenient when using input statistics.

In addition, this strategy is useful for obtaining scaffolds with two-dimensional and three-dimensional gradients. First, 2D-Gyroid1 (G1), 2D-Gyroid2 (G2), and 2D-Gyroid3 (G3) are used to show the generated situations. The interpolation of G1 and G2 is in accordance with a certain law; therefore, an ideal outcome is obtained, as shown in Fig. 9. However, when the volume fraction of the G3 interpolation has no rules, the alteration in the volume fraction is not easily controlled. This problem can be resolved by adding more interpolation points to each dimension. The IWP was selected as the 3D-gradient model to demonstrate the generation of 3D complex structures using the interpolation method, as shown in Fig. 10.

##### 4.2.2. Multisymmetrical TPMS scaffolds

Inspired by the polycrystal-based architectural materials proposed by Chen et al. [47–49], we created a new function for TPMS\_Scaffold\_Generator that enables it to provide STL files of diagonally symmetrical and four-fold symmetrical TPMS scaffolds. Gyroid scaffolds will be used as examples of the design of multisymmetrical TPMS scaffolds. All of them are 20 mm × 20 mm × 20 mm, with a 5-mm unit-cell size and 10% volume fraction.

**4.2.2.1. Diagonally symmetrical TPMS scaffolds.** As mentioned above, the diagonally symmetrical gyroid scaffold can be divided into two sections: one controlled by  $U_G(x, y, z)$  and the other described by  $U_G(-x,$

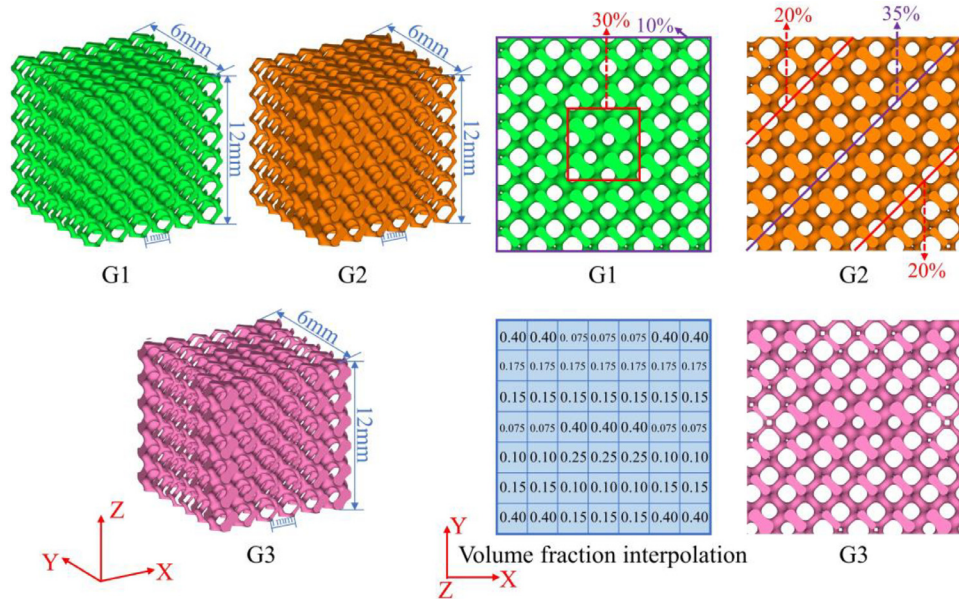
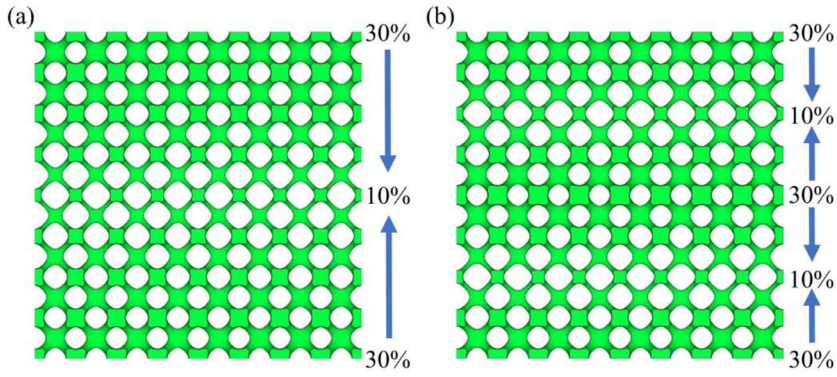


Fig. 9. Stereo plots and top views of G1, G2, and G3.

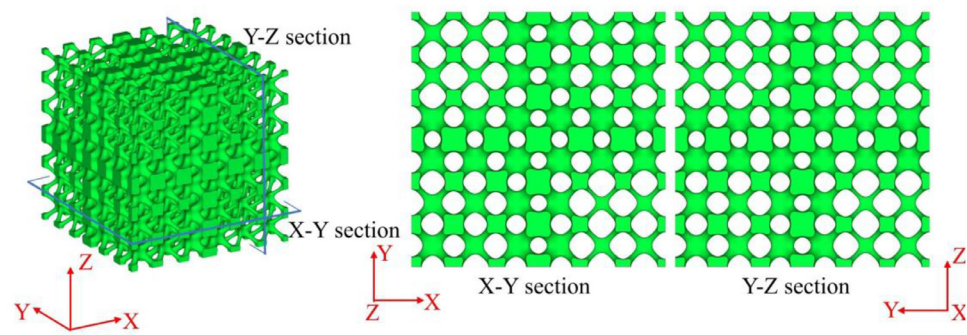


Fig. 10. 3D-IWP scaffold.

$y, z$ ). To smooth the transition of the boundary or symmetry axis, the SF method described in Supporting Information 5 is introduced. Therefore, the diagonally symmetrical gyroid scaffold can be expressed as:

$$U_{two-sym}(x, y, z) = \mu(x, y, z)U_G(x, y, z) + (1 - \mu(x, y, z))U_G(-x, y, z). \quad (2)$$

As shown in Fig. 11(b), the generated diagonally symmetrical gyroid scaffold has two orientations, compared to the uniform gyroid scaffold shown in Fig. 11(a).

#### 4.2.2.2. Four-fold symmetrical TPMS scaffolds.

Building on the diagonally symmetrical TPMS scaffolds, four-fold symmetrical TPMS scaffolds

can be created using the following expression:

$$\begin{aligned} U_{four-sym}(x, y, z) = & \mu(x, y, z)U_{two-sym}(x, y, z) \\ & + (1 - \mu(x, y, z))U_{two-sym}(-x, y, z). \end{aligned} \quad (3)$$

As illustrated in Fig. 11(c), this scaffold has four orientations and three symmetry axes compared with the uniform scaffold.

The method of generating multi-symmetrical scaffolds using TPMS\_Scaffold\_Generator is detailed in Supporting Information Part 6.

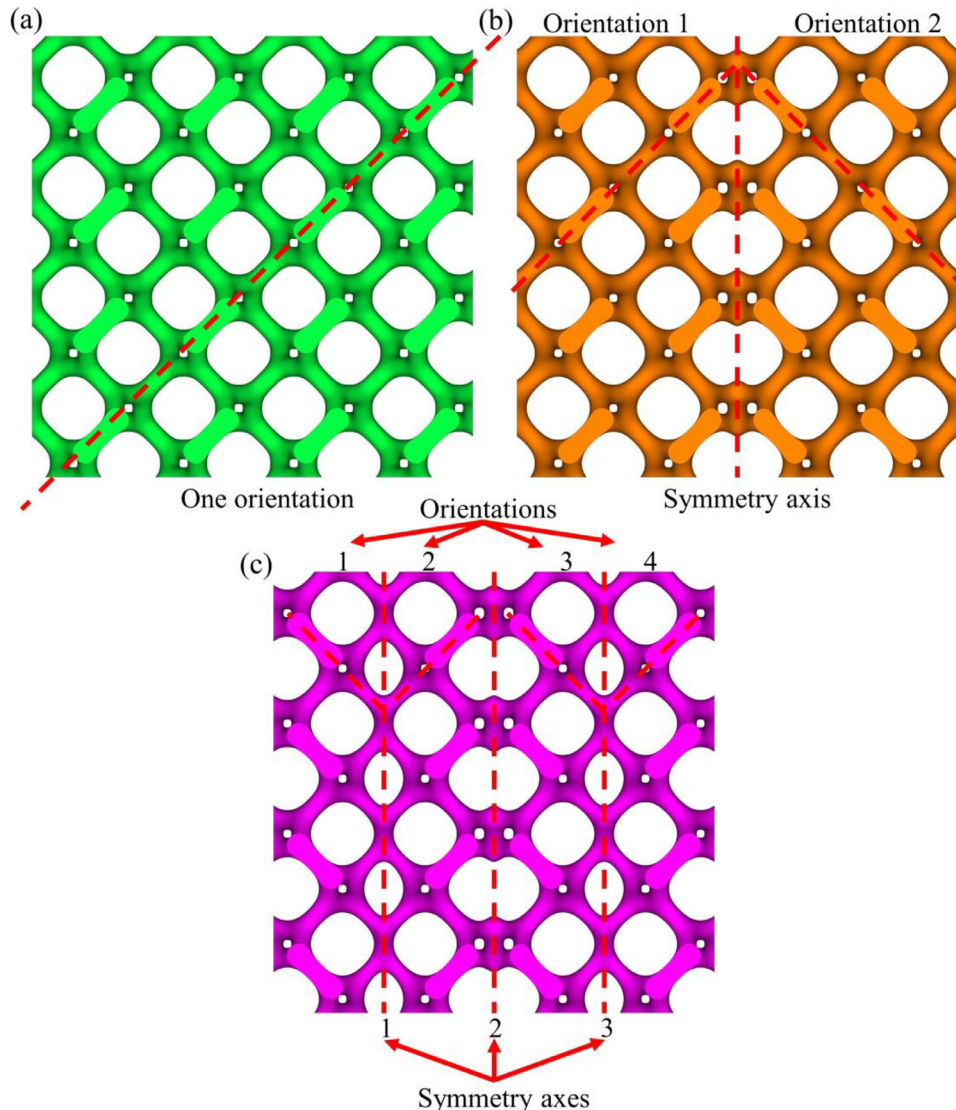


**Fig. 11.** (a) Uniform gyroid TPMS scaffold; (b) Two-fold symmetrical gyroid scaffold with two orientations; (c) Four-fold gyroid scaffold with four orientations.

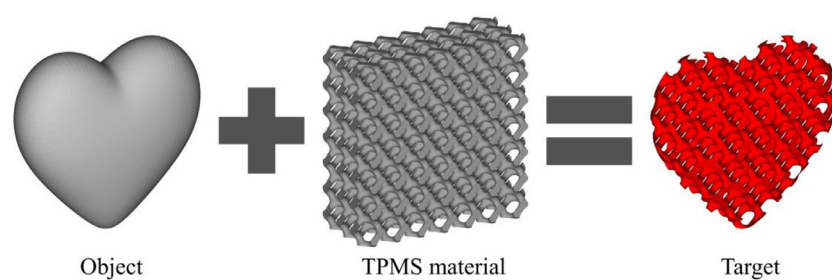


**Fig. 12.** 3D object infilled with TPMS material.

#### 4.3. Scaffolds with different shapes

Scaffolds with different shapes can be easily obtained through Boolean operations in software, such as Materialise Magics. TPMS\_Scaffold\_Generator offers TPMS-based materials to conduct a Boolean operation so that an ideal scaffold can be obtained. The Boolean operation process is illustrated in Fig. 12.

#### 4.4. Transitions between two different scaffolds

In Supporting Information Part 5, an example of the transition shape is only a large plane whose expression is  $Z = C$ . We know that the

transition shape can be changed through  $G(x, y, z)$  from Eq. (S13). As shown in Fig. 13, cylindrical and spherical shapes were used to generate 6 mm × 6 mm × 6 mm multi-morphology scaffolds. In addition, plane transitions can occur along different orientations, as shown in Fig. 13(c).

$$\text{Cylinder: } G_1(x, y, z) = x^2 + y^2 - R^2;$$

$$\text{Sphere: } G_2(x, y, z) = x^2 + y^2 + z^2 - R^2;$$

$$\text{Plane: } G_3(x, y, z) = y - C.$$

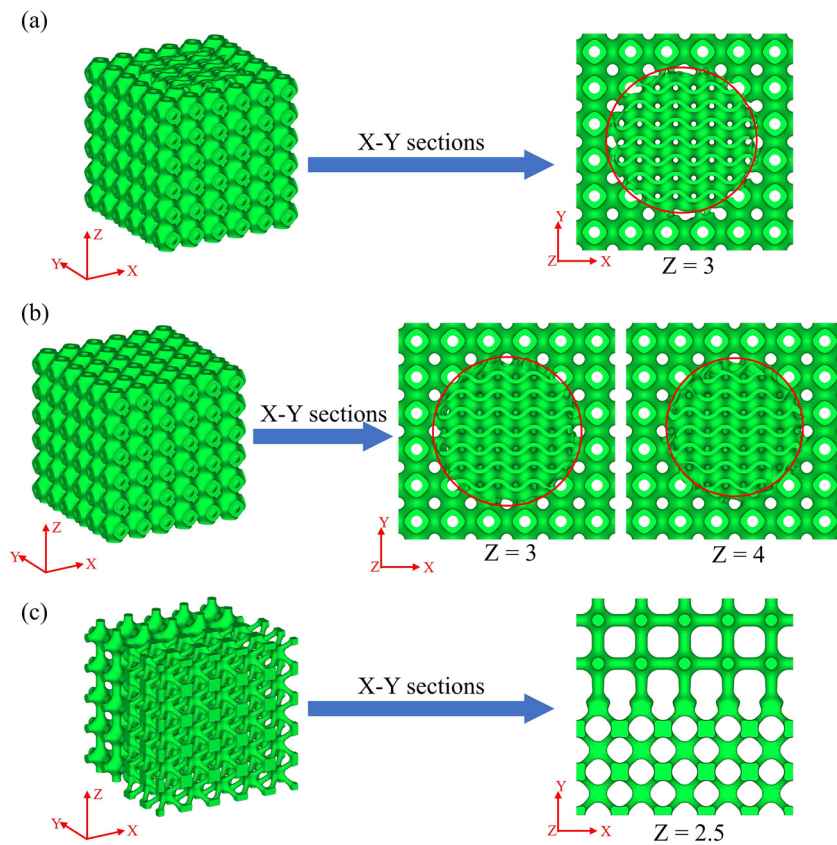


**Fig. 13.** Multi-morphology scaffolds: (a) Cylindrical boundary; (b) Spherical boundary; (c) Plane boundary along y axis.

## 5. Impact Overview and Conclusions

Owing to the vast number of TPMS applications, the generation of scaffold architectures for various applications is a highly studied topic. TPMS\_Scaffold\_Generator provides a free way to create many types of scaffold structures, which cover homogeneous architectures, functionally graded scaffold structures and multisymmetrical scaffolds. Therefore, their mechanical properties and other characteristics can be extensively researched. To better understand these scaffolds, an STL file created by TPMS\_Scaffold\_Generator can be obtained for finite-element analysis.

The generated STL documents can be used effectively to print 3D samples using a wide range of additive-manufacturing techniques. For example, we demonstrated the mechanical properties of  $Ti_6Al_4V$  Fisher-Koch scaffolds. In addition, TPMS\_Scaffold\_Generator offers a new idea for multisymmetrical scaffolds, which can help researchers investigate crack initiation in TPMS scaffolds.

## Declaration of competing interest

The authors declare that they have no known competing financial interests or personal relationships that could appear to influence the work reported in this paper.

## CRediT authorship contribution statement

**Di Lin:** Methodology, Investigation, Formal analysis, Software, Writing – original draft, Visualization. **Cong Zhang:** Writing – review & editing. **Xiyong Chen:** Writing – review & editing. **Nannan Wang:** Writing – review & editing. **Lei Yang:** Methodology, Writing – review & editing, Funding acquisition.

## Acknowledgments

This work was supported by National Natural Science Foundation of China (Grant Nos. 52105396, 52235008, and U2341270), Natural Science Foundation of Hubei Province of China (Grant No. 2021CFB003), Open Foundation of Guangxi Key Laboratory of Processing for Non-ferrous Metals and Featured Materials, Guangxi University, China (Grant No. 2022GXYSOF17), and Fundamental Research Funds for the Central Universities of China (Grant No. 2022IVA138).

## Supplementary materials

Supplementary material associated with this article can be found, in the online version, at doi:10.1016/j.amf.2024.200123.>

## References

- [1] Bhate D, Penick CA, Ferry LA, et al. Classification and selection of cellular materials in mechanical design: Engineering and biomimetic approaches. *Designs* 2019;3(1):19.
- [2] Alomar Z, Concli F. A review of the selective laser melting lattice structures and their numerical models. *Adv Eng Mater* 2020;22(12):2000611.
- [3] Zhang Q, Yang X, Li P, et al. Bioinspired engineering of honeycomb structure—Using nature to inspire human innovation. *Prog Mater Sci* 2015;74:332–400.
- [4] MFy Ashb. The properties of foams and lattices. *Philos Trans Royal Soc A* 1838;364:15–30.
- [5] Gibson LJ. Cellular solids. *MRS Bull* 2003;28(4):270–4.
- [6] Dong Z, Zhao X. Application of TPMS structure in bone regeneration. *Eng Regen* 2021;2:154–62. <http://10.1016/j.engreg.2021.09.004>.
- [7] Al-Ketan O, Rowshan R, Al-Rub RKA. Topology-mechanical property relationship of 3D printed strut, skeletal, and sheet based periodic metallic cellular materials. *Addit Manuf* 2018;19:167–83.
- [8] Yan C, Hao L, Hussein A, et al. Evaluation of light-weight AlSi10Mg periodic cellular lattice structures fabricated via direct metal laser sintering. *J Mater Process Technol* 2014;214(4):856–64.
- [9] Torquato S, Donev A. Minimal surfaces and multifunctionality. *Proc Royal Soc London* 2004;460(2047):1849–56.
- [10] Abueidda DW, Jasik I, Sobh NA. Acoustic band gaps and elastic stiffness of PMMA cellular solids based on triply periodic minimal surfaces. *Mater Des* 2018;145:20–7.

- [11] Liverani E, Lutey AH, Fortunato A, Ascarì A. Characterization of lattice structures for additive manufacturing of lightweight mechanical components. International Manufacturing Science and Engineering Conference, V002T01A012. American Society of Mechanical Engineers; 2017. p. 8. [MSEC2017-2835](http://10.1016/j.msec2017-2835).
- [12] Li K, Chen W, Yin B, et al. A comparative study on WE43 magnesium alloy fabricated by laser powder bed fusion coupled with deep cryogenic treatment: Evolution in microstructure and mechanical properties. *Addit Manuf* 2023;77:103814. <http://10.1016/j.addma.2023.103814>.
- [13] Li K, Ji C, Bai S, et al. Selective laser melting of magnesium alloys: necessity, formability, performance, optimization and applications. *J Mater Sci Technol* 2023;15:65–93. <http://10.1016/j.jmst.2022.12.053>.
- [14] Thomas N, Sreedhar N, Al-Ketan O, et al. 3D printed spacers based on TPMS architectures for scaling control in membrane distillation. *J Membr Sci* 2019;581:38–49.
- [15] Turner MD, Saba M, Zhang Q, et al. Miniature chiral beamsplitter based on gyroid photonic crystals. *Nat Photonics* 2013;7(10):801–5.
- [16] Kim J, Yoo DJ. 3D printed compact heat exchangers with mathematically defined core structures. *J Comput Des Eng* 2020;7(4):527–50.
- [17] Zhu LY, Li L, Li ZA, et al. Design and biomechanical characteristics of porous meniscal implant structures using triply periodic minimal surfaces. *J Transl Med* 2019;17(1):1–10.
- [18] Al-Ketan O, Abu Al-Rub RK. Multifunctional mechanical metamaterials based on triply periodic minimal surface lattices. *Adv Eng Mater* 2019;21(10):1900524.
- [19] Lee W. Cellular solids, structure and properties. *Mater Sci Technol* 2000;16(2):233.
- [20] Yan X, Rao C, Lu L, et al. Strong 3D Printing by TPMS Injection. *IEEE Trans Vis Comput Graph* 2020;26(10):3037–50. <http://10.1109/TVCG.2019.2914044>.
- [21] (2020) Netfabb lattice modules. [Online]: <https://www.autodesk.co.uk/>.
- [22] (2020) Materialise 3-matic. [Online]: <https://www.materialise.com/en/industrial/software/structures>. <https://www.materialise.com/en/industrial/>>software/structures.
- [23] (2020) nTopology. [Online]: <https://ntopology.com/>.
- [24] (2020) Meshmixer. [Online]. Available: <https://www.meshmixer.com/>.
- [25] Maskery I, Parry L, Padrão D, Hague R, Ashcroft I. FLatt pack: A research-focussed lattice design program. *Addit Manuf* 2022;49:102510.
- [26] Marten.(2021) STL lattice generator. [Online]. <https://ww2.mathworks.cn/matlab-central/fileexchange/48373-stl-lattice-generator>.
- [27] Hsieh MT, Valdevit L. Minisurf—A minimal surface generator for finite element modeling and additive manufacturing. *Softw Impacts* 2020;6:100026.
- [28] Al-Ketan O, Abu Al-Rub RK. MSLattice: A free software for generating uniform and graded lattices based on triply periodic minimal surfaces. *Mater Des Process Commun* 2021;3(6):e205.
- [29] Afshar M, Anaraki AP, Montazerian H, et al. Additive manufacturing and mechanical characterization of graded porosity scaffolds designed based on triply periodic minimal surface architectures. *J Mech Behav Biomed Mater* 2016;62:481–94. <http://10.1016/j.jmbbm.2016.05.027>.
- [30] Rajagopalan S, Robb RA. Schwarz meets Schwann: Design and fabrication of biomorphic and durataxic tissue engineering scaffolds. *Med Image Anal* 2006;10(5):693–712. <http://10.1016/j.media.2006.06.001>.
- [31] Schwarz HA. Gesammelte mathematische abhandlungen; 1972.
- [32] Michielsen K, Kole J. Photonic band gaps in materials with triply periodic surfaces and related tubular structures. *Phys Rev B* 2003;68(11):115107.
- [33] Yoo DJ. General 3D offsetting of a triangular net using an implicit function and the distance fields. *Int J Precis Eng Manuf* 2009;10:131–42.
- [34] Wang S, Jiang Y, Hu J, et al. Efficient representation and optimization of TPMS-based porous structures for 3D heat dissipation. *Comput Aided Des* 2022;142:103123.
- [35] Kapfer SC, Hyde ST, Mecke K, et al. Minimal surface scaffold designs for tissue engineering. *Biomaterials* 2011;32(29):6875–82. <http://10.1016/j.biomaterials.2011.06.012>.
- [36] Zhao M, Liu F, Fu G, et al. Improved mechanical properties and energy absorption of BCC lattice structures with triply periodic minimal surfaces fabricated by SLM. *Materials* 2018;11(12):2411.
- [37] Yang L, Mertens R, Ferrucci M, et al. Continuous graded Gyroid cellular structures fabricated by selective laser melting: design, manufacturing and mechanical properties. *Mater Des* 2019;162:394–404. <http://10.1016/j.matdes.2018.12.007>.
- [38] Fu J. Investigating the mechanical performance of the triply periodic minimal surface based metallic lattices made by micro laser powder bed fusion. Hong Kong: The Hong Kong Polytechnic University; 2022.
- [39] Jones A, Leary M, Bateman S, et al. Parametric design and evaluation of TPMS-like cellular solids. *Mater Des* 2022;221:110908.
- [40] Al-Ketan O, Rezgui R, Rowshan R, et al. Microarchitected stretching-dominated mechanical metamaterials with minimal surface topologies. *Adv Eng Mater* 2018;20(9):1800029.
- [41] Al-Ketan O, Rowshan R, Abu Al-Rub RK. Topology-mechanical property relationship of 3D printed strut, skeletal, and sheet based periodic metallic cellular materials. *Addit Manuf* 2018;19:167–83. <http://10.1016/j.addma.2017.12.006>.
- [42] Khoda AKM, Ozbolat IT, Koc B. Designing heterogeneous porous tissue scaffolds for additive manufacturing processes. *Comput Aided Des* 2013;45(12):1507–23. <http://10.1016/j.cad.2013.07.003>.
- [43] Yang N, Zhou K. Effective method for multi-scale gradient porous scaffold design and fabrication. *Mater Sci Eng C Mater Biol Appl* 2014;43:502–5. <http://10.1016/j.msec.2014.07.052>.
- [44] Li Y, Xia Q, Yoon S, et al. Simple and efficient volume merging method for triply periodic minimal structures. *Comput Phys Commun* 2021;264:107956. <http://10.1016/j.cpc.2021.107956>.
- [45] Yang N, Quan Z, Zhang D, et al. Multi-morphology transition hybridization CAD design of minimal surface porous structures for use in tissue engineering. *Comput Aided Des* 2014;56:11–21. <http://10.1016/j.cad.2014.06.006>.
- [46] Yoo DJ, Kim KH. An advanced multi-morphology porous scaffold design method using volumetric distance field and beta growth function. *Int J Precis Eng Manuf* 2015;16(9):2021–32. <http://10.1007/s12541-015-0263-2>.
- [47] Liu C, Lerthanasarn J, Pham MS. The origin of the boundary strengthening in polycrystal-inspired architected materials. *Nat Commun* 2021;12(1):4600. <http://10.1038/s41467-021-24886-z>.
- [48] Zhang C, Qiao H, Yang L, et al. Vibration characteristics of additive manufactured IWP-type TPMS lattice structures. *Compos Struct* 2024;327:117642. <http://10.1016/j.compstruct.2023.117642>.
- [49] Jin J, Wu S, Yang L, et al. Ni-Ti multicell interlacing Gyroid lattice structures with ultra-high hyperelastic response fabricated by laser powder bed fusion. *Int J Mach Tools Manuf* 2023;195:10499. <http://10.1016/j.ijmachtools.2023.104099>.